

Article

Trimetallic Ni-Based Catalysts over Gadolinia-Doped Ceria for Green Fuel Production

Patrizia Frontera ^{1,*}, Anastasia Macario ², Angela Malara ¹, Saveria Santangelo ¹,
Claudia Triolo ³, Fortunato Crea ⁴ and Pierluigi Antonucci ¹

¹ Civil, Energy, Environment and Material Engineering Department, Mediterranean University of Reggio Calabria, 89124 Reggio Calabria, Italy; angela.malara@unirc.it (A.M.); saveria.santangelo@unirc.it (S.S.); pierluigi.antonucci@unirc.it (P.A.)

² Environmental and Chemical Engineering Department, University of Calabria, 87036 Cosenza, Italy; macario@unical.it

³ Mathematical and Computational Sciences, Physics Sciences and Earth Sciences (MIFT), University of Messina, 98122 Messina, Italy; claudia.triolo@unime.it

⁴ Mechanical, Energy and Management Engineering Department, University of Calabria, 87036 Cosenza, Italy; f.crea@unical.it

* Correspondence: patrizia.frontera@unirc.it; Tel.: +39-096-5169-2308

Received: 7 September 2018; Accepted: 29 September 2018; Published: 2 October 2018



Abstract: The present work concerns the characterization of trimetallic nickel catalysts, NiMoRe (Nickel/Molybdenum/Rhenium), NiMoCu (Nickel/Molybdenum/Copper) and NiMoCo (Nickel/Molybdenum/Cobalt), supported on gadolinia-doped ceria and the evaluation of their catalytic performance in the auto-thermal reforming of ethanol to hydrogen. Catalysts have been prepared by wet impregnation and characterized by XRD, SEM-EDX, TG-DSC, TEM, CHNS, H₂-TPR and micro-Raman spectroscopy. The resistance of Ni-alloy catalysts to the carbon deposition and sulfur poisoning has been studied. All catalysts show a similar behavior in the auto-thermal reforming reaction: 100% of ethanol conversion and high selectivity to syngas products, up to 77 vol.%. At 800 °C the coke deposition is very low (less than 0.34 wt%). Sulfur content affects the selectivity and the activity of the catalysts, especially towards the coke formation: high sulfur content promotes the ethylene formation, therefore the amount of coke deposited on spent catalyst increases. NiMoCu seems to be the trimetallic catalyst less sensitive to this aspect.

Keywords: auto-thermal reforming; ethanol; tri-metallic catalyst; nickel; gadolinia-doped ceria; sulfur poisoning

1. Introduction

The world's increasing energy demands makes today biomass an attractive energy source, based on the minimizing of CO₂ emissions and the global warming reduction purposes. Recently, COP-21 (Conference of the Parties), the international meeting on global climate change, defined the roadmap for sustainable worldwide development, based on low-carbon containing fuels. Hydrogen is an energy vector able to substitute the conventional fuels derived from petroleum. Ethanol for hydrogen production represents a valid alternative to the fossil sources due to its low toxicity, low production costs, high biodegradability, high H₂ content, and renewability. Hydrogen derived by bioethanol (or bioethanol directly) can be used in high temperature fuel cells for sustainable and clean power generation. Since 2006, Jamsak et al. [1] have demonstrated the high efficiency of solid-oxide fuel cells (SOFCs) fueled by ethanol. They showed the theoretical performance of SOFCs as a function of electrolyte, mode operation, and water/ethanol ratio [1].

Ethanol conversion to generate hydrogen by a combination of partial oxidation (1) and steam reforming (2) reactions is generally called auto-thermal reforming (ATR).

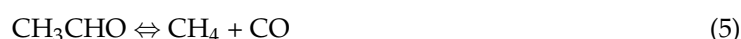


The entire and representative reaction of ATR process can be written as follows:



With respect to the single (1) and (2) reactions, the ATR process is advantageous due to the low energy required and to the reduced carbonaceous deposits formation [2].

This process is characterized by a series of reactions involving organic intermediates or by-products, such as ethylene, methane, and acetaldehyde. In particular, dehydrogenation of ethanol produces acetaldehyde as an intermediate (4) that can be further converted into CH_4 and CO (5). Steam reforming of acetaldehyde (6) and methane could also occur (7) during the process (2).



Moreover, the reaction pathways of ATR of ethanol also involve the decomposition of methane (8) and the CO disproportionation (Boudouard reaction—(9)) reactions that are the causes of the coke formation. Due to the different reaction pathways, the amount of hydrogen varies significantly with the operating temperature. At temperatures ranging between 300 and 500 °C the water gas shift (WGS) reaction (10) could occur, thus increasing the hydrogen production.



In order to favor the WGS reaction and to maximize the hydrogen production, the amount of steam supply is a crucial reaction parameter.

Moreover, the catalyst plays a pivotal role in the ATR process, especially towards the process selectivity and the carbonaceous deposits formation. Several catalytic conversion processes to produce low carbon-containing fuels, such as syngas, synthetic natural gas, and hydrogen, are based on the optimization of the catalyst to maximize the selectivity and the productivity of the final fuel [3–13]. Active species and support have to be selected, synthesized, and combined in order to prepare an active, stable, and economic catalyst.

Noble and nickel-based metals are the active species for ATR reactions. Among noble metals, Rh, Pt, Ru, Ir, and Pd are the most studied, while Al_2O_3 , MgO , La_2O_3 , CeO_2 and ZnO_2 are widely used both as supports for noble metals and nickel [4,14]. Chen et al. deeply investigated the role of noble metals (Ir, Ru, Rh, and Pd) supported on various oxides in the ATR of ethanol, pointing out the attention on the hydrogen selectivity and by-products formation [15]. They found that, even if all noble metals supported on lanthanum showed similar activities, the Ir/ La_2O_3 is the most promising catalyst due to its highest hydrogen selectivity. The same authors, one year later, compared the performance of perovskite-derived catalysts, LaNiO_3 , LaCoO_3 , LaMnO_3 , and LaFeO_3 , with the impregnated Ni/ La_2O_3 in the ATR of ethanol [16]. They found that the LaNiO_3 reduced catalyst is more active with respect

to the impregnated Ni/La₂O₃ due to the better dispersion of Ni particles on the perovskite-derived surface. This improves also the resistance to coke formation and prevents nickel particles sintering.

Nickel is a cost effective alternative solution to the more expensive noble metals, but its activity, in all the dehydrogenation/hydrogenation reactions, must be protected from coke deactivation and sintering phenomena [7,11,12]. In this context, the correct selection of the support, as well as the presence of promoter elements, are fundamental aspects to be considered [17,18]. Very recently, Ghani et al. studied the ATR of crude glycerol over modified ceria-zirconia-supported nickel catalyst with the presence of promoters (Ca, Mg and Gd) [19]. They demonstrated that the Ni/CeZr catalyst promoted with calcium exhibited the highest activity with hydrogen selectivity of c.a. 80%. As confirmed by previous studies [20–22], they observed that the catalyst activity is mostly influenced by the reducibility and Ni dispersion properties. The addition of Na improved also the activity of bimetallic PtRu/ZrO₂ catalyst in the ethanol ATR [22]. Moreover, binary and ternary systems have been tested in different dehydrogenation reactions [23], for capturing simultaneously the positive effects of different metals [24–27].

In Ni-Rh bimetallic catalysts supported on CeO₂, the presence of nickel improves the Rh particles dispersion, leading to higher catalytic activity [24]. Higher stability of RhPt/ZrO₂ with respect to the monometallic catalysts, Pt/ZrO₂ and Rh/ZrO₂, has been observed by Gutierrez et al. at 700 °C for 24 h [25]. Lin et al. studied the ATR of bio-ethanol in a Ni-Pd-Ag alloy membrane reactor [26]. More recently, Wu et al. demonstrated the improvement of catalytic activity and stability of trimetallic NiAuPt/Al₂O₃ catalysts [27]. Particularly, they found that the Ni, Au and Pt form nanoparticles synergistically interacting. This kind of interaction leads to enhance the NiO species reduction, reducing the coke formation and improving the overall catalytic performance. Moreover, by doping the alumina support with MgO or CeO₂ significantly improvement of catalytic performance of monometallic Ni catalyst occurs, while no influence has been detected on the trimetallic catalysts [27]. Bimetallic or trimetallic catalysts, as well as catalysts with doped-promoters supports, may exhibit higher activity, selectivity and stability with respect to the corresponding monometallic ones.

However, the preparation method also affects the final catalysts performance. Among the preparation methods of supported catalysts, i.e., wetness impregnation, dry impregnation, sol-gel, ammonia evaporation, deposition/precipitation, and co-precipitation, the most used is wetness impregnation. Impregnation is a simple and economic method by which is possible to obtain a reproducible metal loading on the support surface. The catalyst preparation method strongly influences the metal particles size and dispersion, as well as the interaction between metal and support and, consequently, the reducibility and thermal stability of the final catalyst [28–32].

In addition, the tolerance of catalysts to the various impurities present in the bioethanol should be improved in order to preserve their stability. Among the impurities present in the crude bio-ethanol, hydrogen sulfide is the main poisonous for the catalyst. Direct use of bio-ethanol or hydrogen derived by bioethanol in technologies for energy conversion, such as SOFCs, could cause problems related to sulfur poisoning [32]. Purification processes can be applied to the fuel before passing into the SOFC but the costs of the system surely increase. Reduction of system costs is always desired. For this reason, the worldwide ongoing researches focus on the development of catalytic material simultaneously able to preventing the formation of coke and resisting sulfur poisoning [33].

Toward this route, the present work reports on the development of efficient and tolerant materials, to sulfur poisoning and coke deposition, made by gadolinium-doped ceria (GDC), as support, and ternary Ni-alloys, as active phases. Synthesized material can be considered an alternative material for efficient SOFCs anode. The GDC is able to combine the effects of ceria with those of rare earths, resulting in a material with “self de-coking” capability [5]. In particular, in our previous study we have demonstrated the ability of ceria to generate oxygen vacancies, able to weaken the carbon-oxygen bond of CO₂ adsorbed on metal sites and to increase the dissociation of CO₂. Simultaneously, the presence of rare heart, like gadolinia, improves the basicity of the support, improving the CO₂ adsorption and reducing the coke deposition [5].

Moreover, several experimental studies demonstrated the beneficial effects of the alloying elements on the fuel cell performance [34,35]. In particular, Cu/Ni and Co/Ni anode catalysts were found to be the most active while Mo/Ni alloy was predicted to be the most resistant to the C and S deposition [30]. On the other hand, it is well known that Mo and Co are the most used metals in the catalysts for the Claus process for the conversion of hydrogen sulfide to sulfur [36,37].

In this work, NiMoRe/GDC, NiMoCu/GDC, and NiMoCo/GDC catalysts have been prepared by impregnation method, characterized by different analytical techniques (XRD, TEM, TG-DSC, SEM-EDX, CHNS, H₂-TPR, and micro-Raman spectroscopy) and tested in the ATR of ethanol, in the temperature range 500–800 °C, with or without H₂S in the fuel feed. The analytical investigation has been focused on preventing the coke deposition, the metals sintering effect and the sulfur poisoning. Hydrogen productivity, ethanol conversion and products distribution have been measured and analyzed.

2. Results and Discussion

2.1. Catalysts Characterization Results

The XRD patterns of calcined and reduced catalysts, NiMoRe/GDC, NiMoCu/GDC, and NiMoCo/GDC, are shown in Figures 1–3. The support pattern presents the characteristic features of cerium oxide doped with gadolinia having a fluorite-like structure [38]. In the NiMoCu/GDC (Figure 1) the support remains unaltered after calcination (Figure 1, spectrum b) and reduction (Figure 1, spectrum c); nonetheless, the sharpening of the peaks related to the support indicates the growing of crystallite grains of support.

In the pattern of calcined NiMoCu/GDC (Figure 1, spectrum b) different peaks attributable to different metal oxide phases are present. The little peak at 26.4° 2θ is attributable to the β-phase of nickel molybdate (JCPDS powder diffraction file card no. 33-948); despite this is a metastable phase, it was detected in the diffractogram of the catalysts calcined at 800 °C (characteristic peak at 26.88° 2θ), which suggests that the support plays a role in the stabilization of this phase [39]. The peaks (spectrum b, Figure 1) at 37.28°, 43.37°, 62.90° 2θ correspond to NiO (JCPDF File 78-0643); after reduction, they disappear in the relative pattern (spectrum c, Figure 1). The peak of metallic nickel is present (spectrum c) at 44.5° 2θ (JCPDF File 45-1027). In the calcined sample, no peaks attributable to copper phases are detected; however, in the pattern c a little peak at 50.89° 2θ could be ascribed to metallic copper (JCPDF File 04-0836).

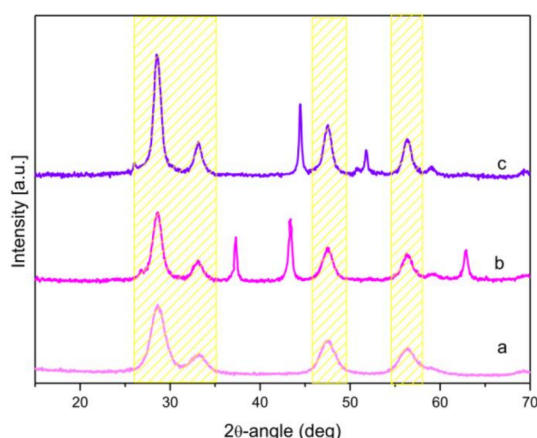


Figure 1. X-ray patterns of: gadolinium-doped ceria (GDC) support (spectrum a)—NiMoCu/GDC sample after calcination (spectrum b), and after reduction (spectrum c). Features arising from the GDC support are yellow-highlighted.

Regarding the NiMoCo/GDC catalyst, the comparison of pattern of the support with the patterns of calcined and reduced catalysts (Figure 2, spectra b and c) suggests the occurrence of segregation of the support into individual oxide phases (CeO₂ and Gd₂O₃) highlighted by the presence of shoulders

on the peaks related to the support. The signals for CeO_2 and Gd_2O_3 arise at 2θ values of 28.6° , 33.5° , 48.0° , 57.0° and 19.8° , 29.2° , 32.82° , 52.8° , respectively (JCPDS File 43-1014).

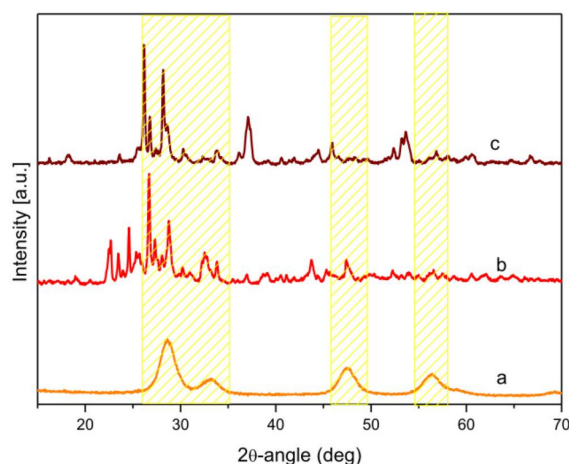


Figure 2. X-ray patterns of: GDC support (spectrum a)—NiMoCo/GDC sample after calcination (spectrum b), and after reduction (spectrum c). Features arising from the GDC support are yellow-highlighted.

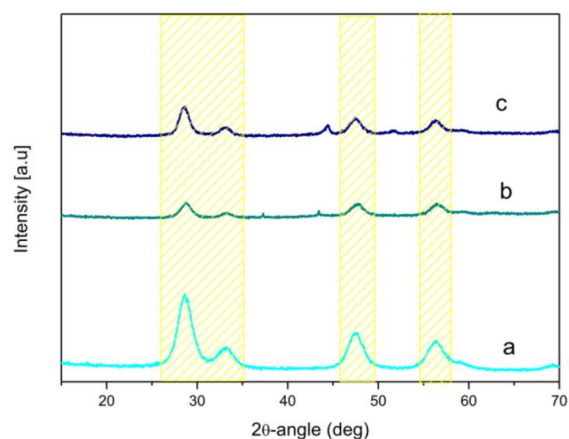


Figure 3. X-ray patterns of: GDC support (spectrum a)—NiMoRe/GDC sample after calcination (spectrum b), and after reduction (spectrum c). Features arising from the GDC support are yellow-highlighted.

This destabilizing effect (segregation in the two oxide phases) has been previously observed for ceria-zirconia supported catalysts loaded with nickel and cobalt salt, and however the detrimental effect on support did not affect the catalytic performance of the catalyst [40]. The presence of other numerous peaks is attributable to the contemporary presence of cobalt oxide (PDF 00-043-1003), molybdenum oxide (PDF 00-012-0517) and to a mixed oxide (nickel molybdenum oxide, PDF 00-033-0948). The reduction step performed at $T = 650^\circ\text{C}$ does not fully achieve the goal of reducing metal oxide and obtaining active metallic particles, as confirmed by TPR analyses (see below).

In the NiMoRe/GDC catalysts, the support maintains the original structure after both thermal treatments (Figure 3, spectra b, c); however, a loss of intensity is observed.

No relevant shrinkages in the peaks of the support were observed, then no agglomeration of particles support is envisaged.

Despite the high loading of metals, with the exception of nickel species, in the calcined and reduced form no other metals species related to molybdenum or rhenium have been detected in the samples, suggesting that both metals are highly dispersed with very small particle size [41].

The amount of metals on the catalysts has been measured by SEM-EDX technique. The results confirm that the metals amount on the final catalyst is very close to the nominal value for all prepared

samples. Elements mapping also shows that the metals are uniformly dispersed onto the support (see Figures S1 and S2 in the Supplementary Information).

The TEM images of reduced catalysts are reported in Figure 4. It is possible to observe well-dispersed metals particles, with dimension ranging between 6 and 10 nm, without formation of metals agglomerates, agreeing well the SEM results. The GDC support has an average dimension of ca. 90 nm (measure showed in Figure 4c, as representative sample).

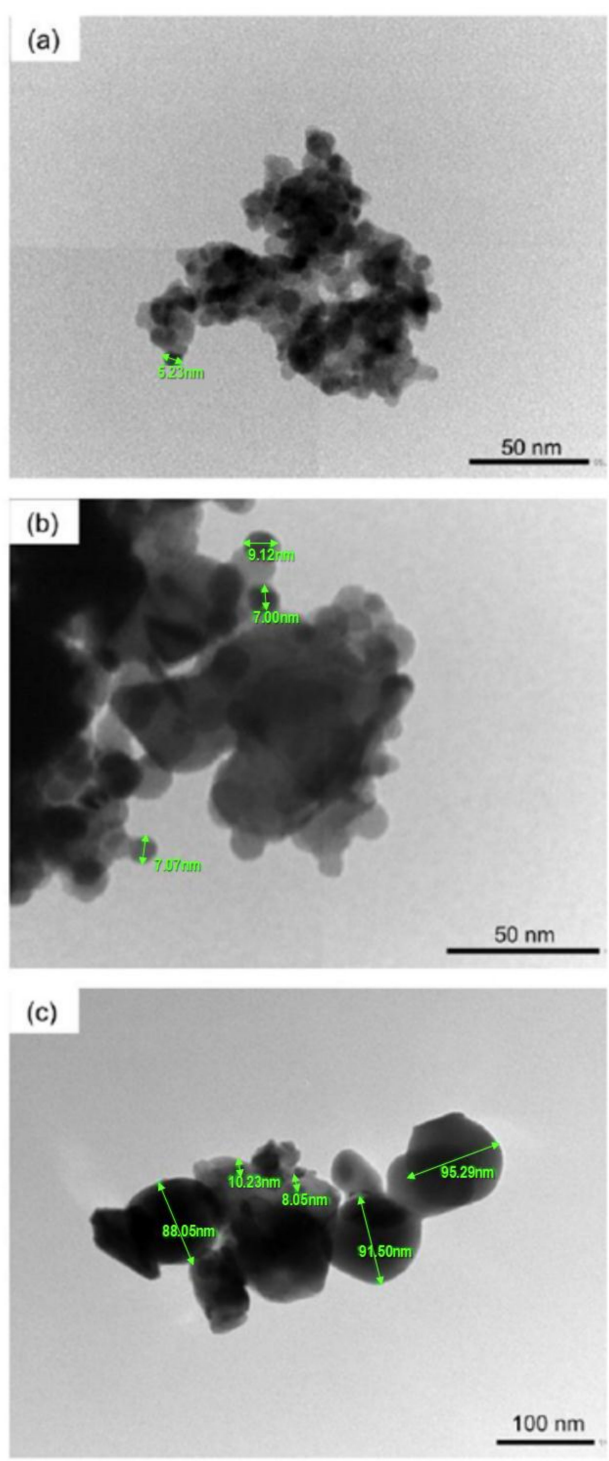


Figure 4. TEM images of reduced catalysts: (a) NiMoRe/GDC, (b) NiMoCu/GDC, (c) NiMoCo/GDC.

The reductive ability of the catalysts precursors was studied by H₂-TPR; the results are presented in Figure 5.

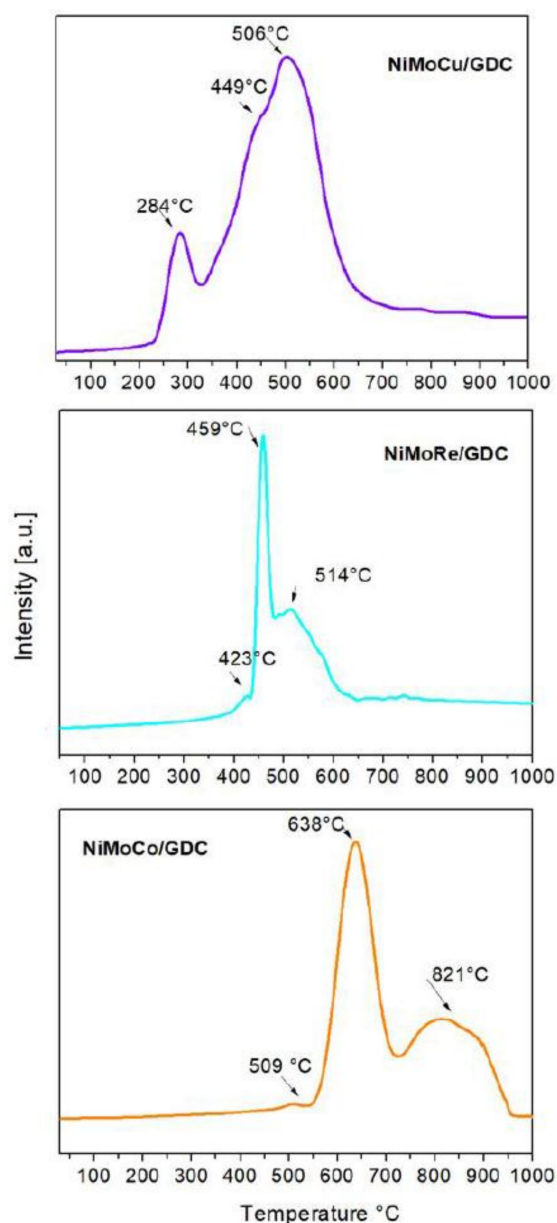


Figure 5. H₂-TPR profiles of trimetallic catalysts.

NiMoCu/GDC and NiMoRe/GDC are the catalysts with higher reducibility, in agreement with XRD patterns of the reduced samples (Figure 1 spectrum c and Figure 3 spectrum c), where no diffraction peaks of oxide species are present. Instead, for NiMoCo/GDC it is possible to observe that the activation temperature ($T = 650$ °C) is not suitable to obtain a complete reduction of the catalyst. This is also confirmed by XRD pattern (Figure 2 spectrum c), in which oxides species were detected.

For all TPR profiles, three major peaks are present. In the spectrum of NiMoCu/GDC the first peak ($T = 284$ °C) can be attributed to copper ions and to the metallic species that weakly interacts with the support [42].

The second peak ($T = 449$ °C) is a shoulder of the larger one that can be attributed to metallic nickel; the third peak ($T = 506$ °C) is ascribed to metallic molybdenum. The broadening of these peaks envelopes all types of the metallic species, both those strongly linked to the support and those that interact weakly [43,44].

The TPR profile of NiMoRe/GDC exhibits well defined peaks; the first peak ($T = 423\text{ }^{\circ}\text{C}$) is attributable to rhenium [45], the other two peaks can be ascribed to nickel ($T = 459\text{ }^{\circ}\text{C}$) and to molybdenum species ($T = 514\text{ }^{\circ}\text{C}$).

The presence of cobalt in the NiMoCo/GDC catalyst promotes the shift of the peaks attributable to nickel ($T = 638\text{ }^{\circ}\text{C}$) and to the molybdenum metallic species ($T = 821\text{ }^{\circ}\text{C}$) towards higher temperatures, in agreement with E. Rodriguez- Castellon et al., which reported the addition of cobalt to molybdenum retarded the reducibility of this latter [46].

2.2. Auto-Thermal Reforming of Ethanol: Catalytic Tests

Figure 6 shows the average products distribution, for each catalyst, obtained after 10 h at 600 and 800 $^{\circ}\text{C}$, without hydrogen sulfide. For all catalysts the ethanol conversion was complete (100%). At both temperatures tested, the main products are hydrogen and carbon monoxide; significant amounts of unconverted methane, CO_2 , and ethylene, as by-products, were also present.

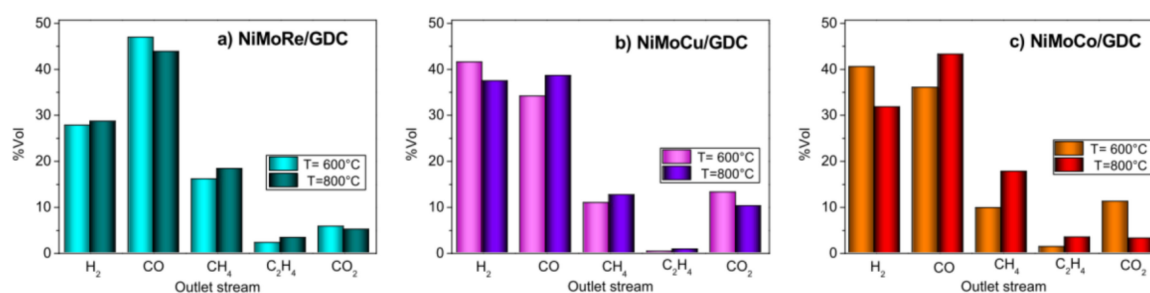


Figure 6. Products distribution of auto-thermal reforming (ATR) reaction catalyzed by: (a) NiMoRe/GDC, (b) NiMoCu/GDC, (c) NiMoCo/GDC catalysts, after 10 h and 120,000 h^{-1} space velocity.

The main product in the reaction catalyzed by NiMoRe/GDC is carbon monoxide, both at 600 $^{\circ}$ and 800 $^{\circ}\text{C}$ (Figures 6a, 7 and 8), while for NiMoCu/GDC and NiMoCo/GDC catalysts H_2 is the main product at 600 $^{\circ}\text{C}$ (Figure 6b,c and Figure 7). At 800 $^{\circ}\text{C}$ NiMoCu/GDC allows to obtain the 37% of H_2 and the 38% of CO (Figures 6b and 8). For NiMoCo/GDC, CO is the main product at 800 $^{\circ}\text{C}$ (Figures 6c and 8). The higher selectivity to CO at 800 $^{\circ}\text{C}$ observed for NiMoRe/GDC and NiMoCo/GDC is ascribable to the occurrence of reverse water gas shift reaction (RWGS, $\text{CO}_2 + \text{H}_2 \rightleftharpoons \text{CO} + \text{H}_2\text{O}$), which is favored at temperatures higher than 700 $^{\circ}\text{C}$. This suggests that NiMoCu/GDC is able to reduce the consumption of H_2 by the RWGS reaction. Therefore, the NiMoCu/GDC catalyst shows the best selectivity to hydrogen.

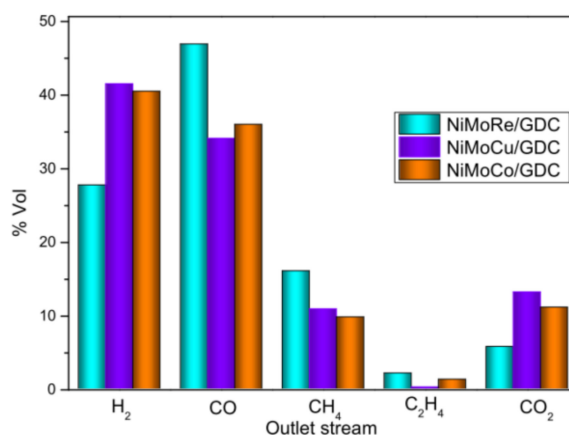


Figure 7. Comparison of products distribution of ATR reaction catalyzed by different catalysts, after 10 h, 120,000 h^{-1} space velocity, and 600 $^{\circ}\text{C}$.

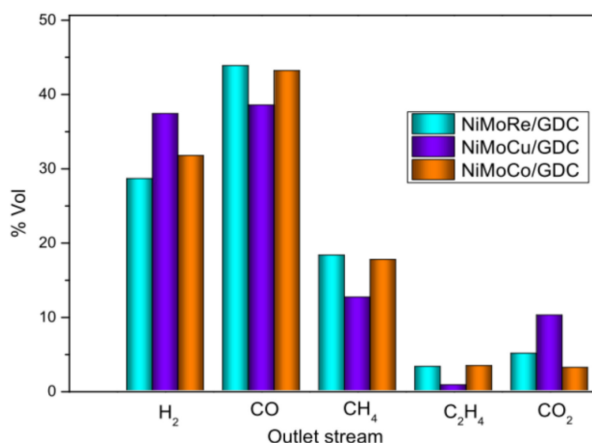


Figure 8. Comparison of products distribution of ATR reaction catalyzed by different catalysts, after 10 h, 120,000 h⁻¹ space velocity, and 800 °C.

In any case, the selectivity of catalysts towards syngas (H₂ + CO) is not affected by the temperature reaction (see Figure S3 in the Supplementary Information): for all catalysts the total amount of syngas ranged between 72 and 77 vol%.

The effect of sulfur on the selectivity of catalysts to syngas is reported in Figure 9. The addition of sulfur has a similar impact on the performance of all the catalysts tested. In particular, the addition of 100 ppm H₂S reduces effectively the production of syngas, even if no catalysts deactivation is apparent: ethanol conversion is still complete after 10 h of reaction at 800 °C. Increasing the hydrogen sulfide content in the feed, up to 200 ppm, the ethanol conversion does not change, while the selectivity to syngas slowly increases. The NiMoCu/GDC catalyst showed the best resistance to sulfur poisoning: with the addition of 200 ppm H₂S the syngas production decreases of about 12%, while for NiMoRe/GDC the decrease is of about 15%; for NiMoCo/GDC is of ca. 17%.

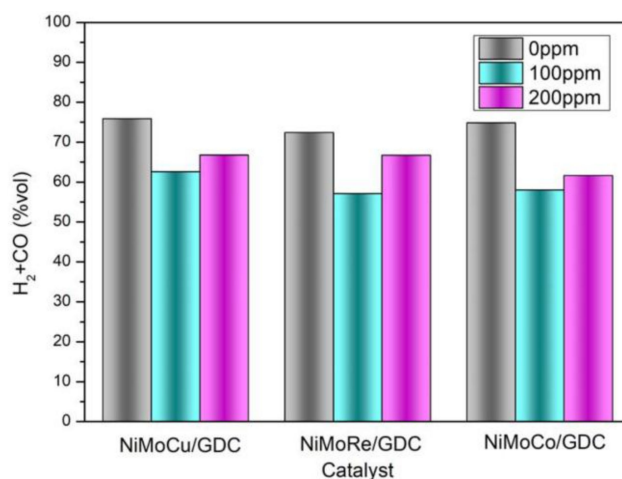


Figure 9. Sulfur impact on the syngas selectivity of catalysts (800 °C, 10 h, 120,000 h⁻¹ space velocity).

Figure 10 provides information on the composition of the outlet stream. It is evident that the presence of sulfur in the inlet stream causes the decrease in the yield of syngas.

However, the sulfur impact on the products distribution should be explained together with the analysis of coke deposition results [47]. For this reason, a more deepened discussion on the sulfur impact on catalysts performance is postponed to the following section.

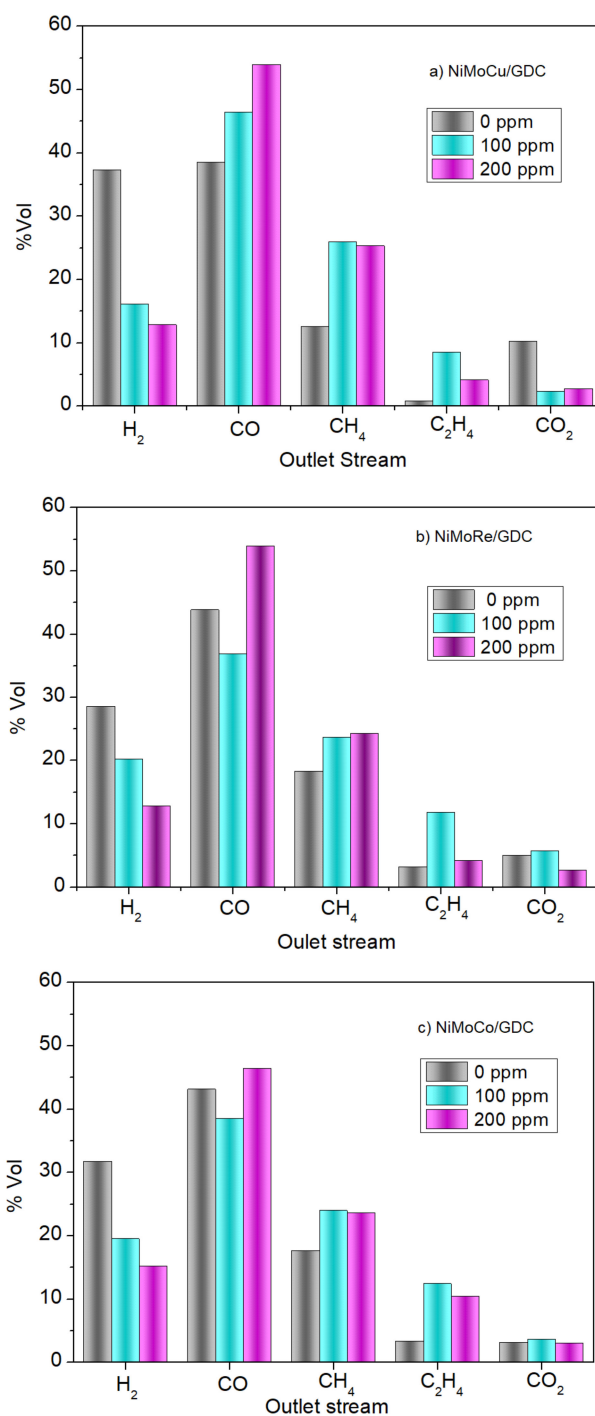


Figure 10. Sulfur impact on products distribution of auto-thermal reforming catalyzed by: (a) NiMoCu/GDC, (b) NiMoRe/GDC, (c) NiMoCo/GDC, (800 °C, 10 h, 120,000 h⁻¹ space velocity).

2.3. Characterization of Spent Catalysts

2.3.1. Coke Deposition and Sulfur Impact

Table 1 reports the amount of coke deposited on the catalyst after reaction, measured by TG-DSC. The TG-DSC profiles of the spent catalysts exhibit a similar behavior, with the presence of an exothermic peak in the DSC curve at about 600 °C, corresponding to the combustion of deposited coke (see Figure S4 in the Supplementary Information). The presence of coke has been also detected in the XRD spectra

of all spent catalysts in which the amount of coke deposited was higher than 5 wt% (see Figure S5 in the Supplementary Information).

Table 1. Coke amount over catalysts after reaction in presence of H₂S, measured by TG-DSC analysis.

Catalysts	Coke Amount (wt%)			
	600 °C		800 °C	
	Without H ₂ S	Without H ₂ S	100 ppm of H ₂ S	200 ppm of H ₂ S
NiMoCu/GDC	23.7	0.10	5.46	5.48
NiMoRe/GDC	29.8	0.25	0.62	2.94
NiMoCo/GDC	26.3	0.34	7.63	9.69

The amount of coke produced at 600 °C was higher than that deposited after reaction at 800 °C. This is ascribable to the exothermic reverse-Boudouard reaction ($2\text{CO} = \text{C} + \text{CO}_2$, $\Delta H_{298\text{K}} = -172.4$ kJ/mol), which is favored at temperatures lower than 700 °C [48]. In the presence of H₂S at $T = 800$ °C, the amount of coke produced increases for all catalysts; NiMoCu/GDC is less affected by the increase of H₂S amount from 100 to 200 ppm, with respect to the other two catalysts (Table 1).

The lower catalyst deactivation by coke deposition could be explained by the effect of sulfur content on the products distribution (Table 2 and Figure 11). Hydrogen and ethylene contents as reaction products are strongly affected by the sulfur content in the inlet stream; in particular, the hydrogen amount decreases with sulfur content increasing, while ethylene initially increases (in presence of 100 ppm of H₂S) and subsequently decreases (in presence of 200 ppm of H₂S).

It is well known that ethylene can be produced from ethanol by dehydration reaction ($\text{C}_2\text{H}_5\text{OH} = \text{C}_2\text{H}_4 + \text{H}_2\text{O}$) and is one of the hydrocarbons more prompt to form coke [49]. According to this aspect, at 800 °C, in the presence of 100 ppm of H₂S, we observed that the ethylene in the reaction products increases (Table 2 and Figure 11) and, consequently, the coke formation increases too. Production of ethylene by dehydrogenation, is known promoted by the presence of acid sites [47,50], therefore it is plausible that the increase in H₂S favors the formation of ethylene. Consequently, the coke formation is correlated to the lower selectivity of the catalysts to hydrogen.

When the amount of H₂S increases again, from 100 ppm to 200 ppm, the ethylene concentration in the products decreases but the coke amount continues to increase.

The TEM images of spent NiMoRe/GDC catalyst (as a representative sample) after 10 h of reaction at 800 °C without sulfur and with 200 ppm H₂S in the inlet gas, are reported in the Figure 11. After reaction without sulfur, the catalyst surface is very clean and the coke quantity is negligible, as confirmed by thermal analysis (0.25 wt%). On the contrary, after reaction with 200 ppm H₂S, a great amount of deposited carbon, in amorphous form, is clearly visible on the surface of the spent catalyst.

Table 2. Coke amount over catalysts after reaction in presence of H₂S, measured by TG-DSC analysis at 800 °C.

Catalysts	Coke Amount (wt%)			C ₂ H ₄ (vol.%)			H ₂ (vol.%)		
	Without H ₂ S	100 ppm of H ₂ S	200 ppm of H ₂ S	Without H ₂ S	100 ppm of H ₂ S	200 ppm of H ₂ S	Without H ₂ S	100 ppm of H ₂ S	200 ppm of H ₂ S
NiMoCu/GDC	0.10	5.46	5.48	0.74	8.51	4.12	37.36	16.10	12.81
NiMoRe/GDC	0.25	0.62	2.94	3.24	11.83	4.19	28.59	20.26	12.80
NiMoCo/GDC	0.34	7.63	9.69	3.34	12.41	10.46	31.70	19.50	15.20

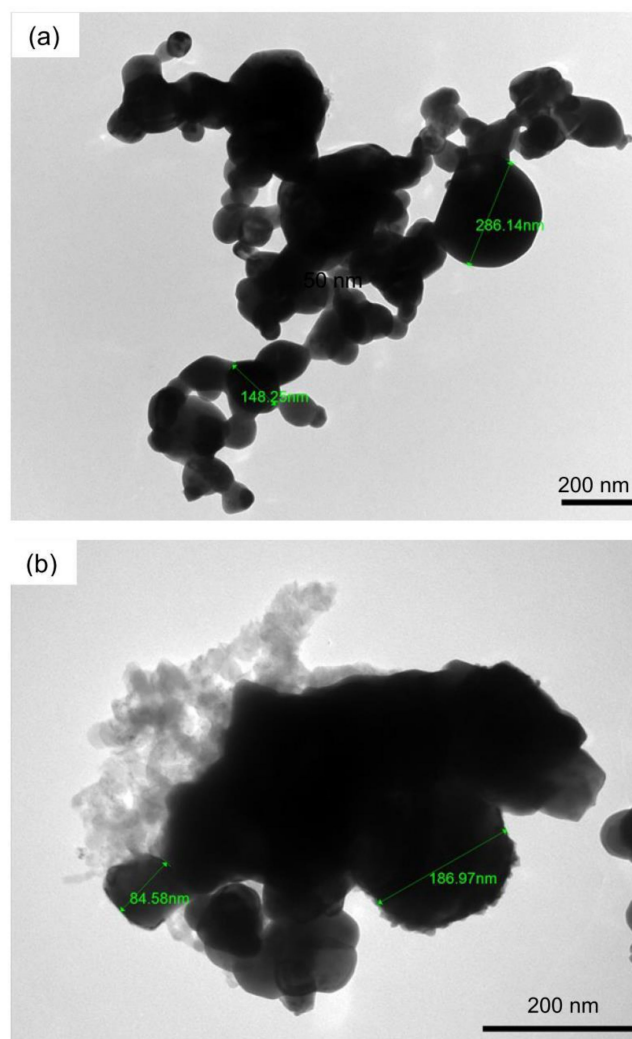


Figure 11. TEM image of spent NiMoRe/GDC catalyst (a) without H₂S and (b) with H₂S after 10 h of reaction at 800 °C without H₂S.

This behavior could be due to the fact that the increase of H₂S to 200 ppm in the feed does not mean that the acidity of catalysts increases simultaneously. Moreover, no sulfur evidence on the catalyst surface after reaction is apparent by CHNS analysis.

Therefore, the amount of ethylene does not increase, but the activity of catalysts decreases due to the poisoning effect of the high sulfur content, then hydrogen production decreases as coke increases. This phenomenon is less evident for NiMoCu/GDC catalyst and suggests that this latter is less sensitive to the presence of sulfur.

2.3.2. Coke Speciation by Micro-Raman Spectroscopy

Raman spectroscopy is a non-destructive characterization technique, widely utilized to study structural and bonding properties of all the carbon species [51–53]. Figure 12 displays micro-Raman spectra typically measured on GDC-supported catalysts after ATR of ethanol at 800 °C with different H₂S concentrations in the feed. The Raman fingerprint of disordered C_{sp}²-based materials is present in all the spectra. The detection of the D- and G-bands (centered at 1321–1326 cm⁻¹ and 1582–1593 cm⁻¹, respectively) proves that disordered carbonaceous deposits always form on the catalyst surface, regardless of H₂S concentration (100 or 200 ppm) and type of the metal-catalyst (NiMoRe/GDC, NiMoCu/GDC or NiMoCo/GDC). Indeed, a fair correlation is found between the average intensity of

the Csp^2 related bands and the relative amount of deposited carbon, as assessed by thermo-gravimetric analysis (Figure S6).

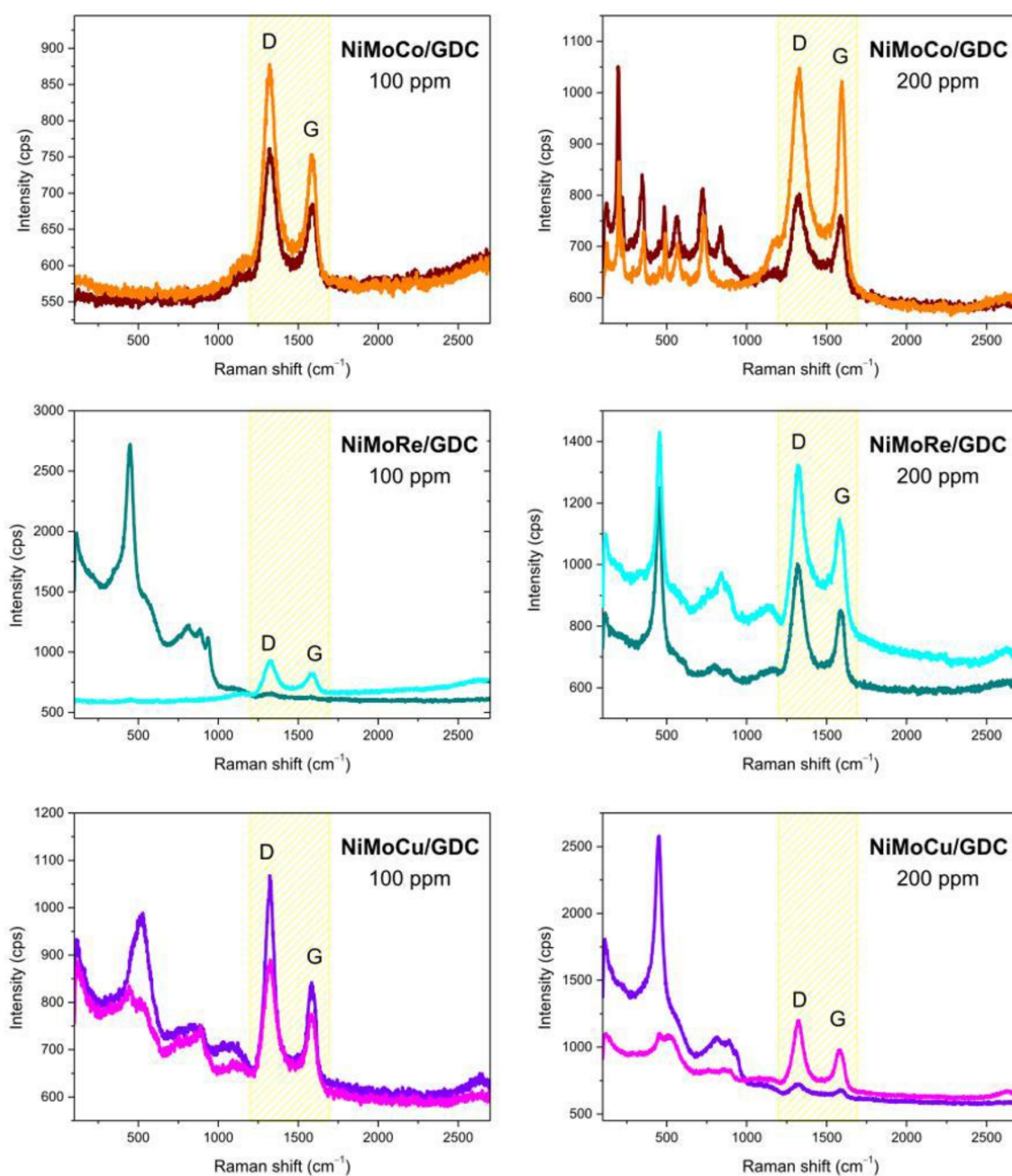


Figure 12. Micro-Raman spectra of the exhaust catalysts after ATR of ethanol at 800 °C with different H_2S concentrations, as-measured in two different locations of each specimen. Features arising from the Csp^2 related bands of deposited carbon are yellow-highlighted.

In order to investigate the spatial homogeneity of carbon deposits, spectra were recorded at different locations in each of the investigated catalysts. Different spectral profiles are indicative of the lack of spatial homogeneity, with carbonaceous deposits being locally thicker where the relative intensity of the Csp^2 bands is stronger. In the case of NiMoCo/GDC catalysts, for fixed H_2S concentration, the spectral profile does not significantly change point by point, indicating that coke deposits uniformly all over the catalyst surface. However, at the lower H_2S concentration, a thicker coke layer coats the catalyst surface hindering the detection of the Raman modes arising from the catalyst. In the case of NiMoRe/GDC and NiMoCu/GDC catalysts, spatial uniformity of the

carbonaceous deposits depends on the H₂S concentration. In the former catalyst the thickness of the coke layer results to be spatially non-uniform at the lower H₂S concentration, in the latter the opposite situation occurs.

Aiming at clarifying the nature of the carbonaceous deposits, the spectra were quantitatively analyzed by a fitting procedure. The main parameters obtained are shown in Figure 13a–e.

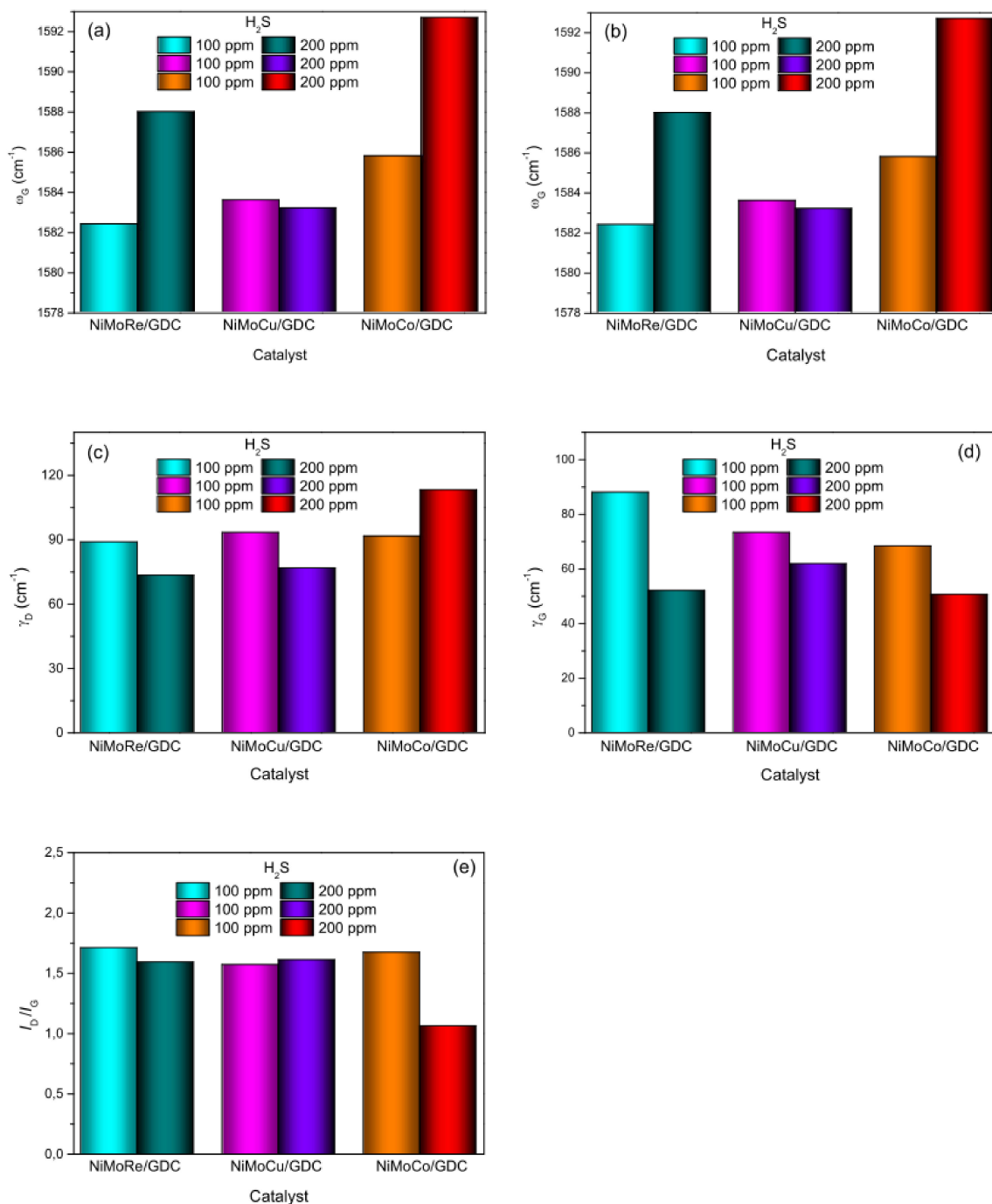


Figure 13. (a,b) Center frequencies (ω_D and ω_G) and (c,d) widths (γ_D and γ_G) of the D- and G-bands and (e) D/G intensity ratio (I_D/I_G) in the investigated catalysts for different H₂S concentrations.

The D-band is usually assigned to *K*-point phonons of *A*_{1g} symmetry, whereas the G-band is attributed to the zone-center phonons of *E*_{2g} symmetry. The former originates from the breathing

modes of ring-organized C-atoms. The latter is associated to the in-plane bond stretching of all the pairs of (both ring- and chain-organized) C-atoms [54,55].

The D-mode is forbidden in perfect graphite. It becomes Raman-active in the presence of finite size effects, dangling-bonds, vacancies, grain boundaries, distorted hexagons, pentagon-heptagon pairs or other in-plane topological defects, which breaking the basic translational graphene-layer symmetry, relax the selection rules [54,55]. For fixed excitation energy, D-band intensifies with decreasing in-plane correlation length [51,53–55] (i.e., mean inter-defect distance [55,56]). Thus, the D/G intensity ratio (I_D/I_G) commonly monitors the amount of structural defects, or the extent of deviation of the crystalline arrangement from a perfect hexagonally organized planar C network. Any increase of the crystalline order in the Csp^2 lattice (graphitization) is accompanied by a decrease in I_D/I_G [53].

Ratio of tetrahedral- to trigonal-bonds, clustering of the sp^2 phase, bond disorder and organization of Csp^2 atoms (rings or chains) cooperate in determining the shape of the Raman spectra of disordered/amorphous carbons. The G-band band-width (γ_G) is commonly regarded as a measure of the homogeneous disorder related with the statistical distribution of bond angles; its center position (ω_G) may increase as an effect of sp^3/sp^2 bonding fraction diminishing, clustering enhancement, bond-angle disorder reduction and presence of Csp^2 atom chains [56–58]. Thus, in the NiMoCu/GDC catalyst nature and microstructure of the carbonaceous deposits seems to be relatively insensitive to the changes in H_2S concentration. In fact, the shape of Csp^2 -related spectral features, as described by the parameters displayed in Figure 13, does not largely change with varying H_2S concentration.

On the contrary, in NiMoRe/GDC and NiMoCo/GDC catalysts the G-band up-shifts and shrinks with increasing H_2S concentration (Figure 13b,d, respectively), hinting at a reduction of the homogeneous disorder. In the NiMoCo/GDC catalyst these spectral changes are accompanied by the decrease of I_D/I_G (Figure 13e), which indicates that more structurally ordered C nanostructures form on its surface with 200 ppm H_2S .

This consideration is confirmed by TEM image of spent NiMoCo/GDC catalysts where carbon nanotubes are clearly visible (Figure 14).

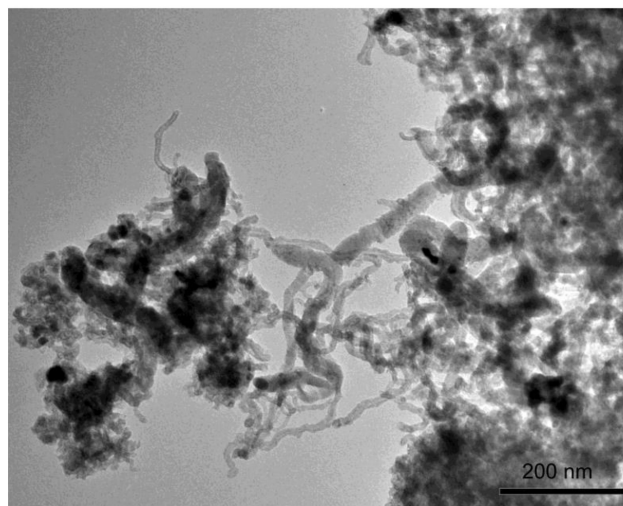


Figure 14. TEM images of spent NiMoCo/GDC catalyst at different magnification.

The formation of disordered carbons (“coke”) on the surface of exhaust (“coked”) catalysts causes the catalyst to deactivate [52,59]. The G-band center frequency strongly depends on the nature of coke [58]. For mainly olefinic coke ω_G lies above 1600 cm^{-1} , whereas if the coke is mainly aromatic, as in the present case, ω_G is located below 1600 cm^{-1} . Therefore, it is concluded that the decomposition of ethanol in presence of sulfur produces aromatic coke on the surface of all the catalysts, observed also by other authors [60]. Varying H_2S concentration (100 or 200 ppm) and type of the metal-catalyst

(NiMoRe/GDC, NiMoCu/GDC or NiMoCo/GDC) gives rise only to changes in spatial uniformity and thickness (i.e., amount) of the carbonaceous deposits.

3. Experimental Section

3.1. Catalyst Preparation

Trimetallic catalysts were prepared by wet co-impregnation procedure. The metal sources (nickel nitrate hexahydrate $\text{Ni}(\text{NO}_3)_2 \cdot 6\text{H}_2\text{O}$, Ammonium molybdate tetrahydrat $(\text{NH}_4)_6\text{Mo}_7\text{O}_{24} \cdot 4\text{H}_2\text{O}$, Copper(II) nitrate hemi(pentahydrate) $\text{Cu}(\text{NO}_3)_2 \cdot 2.5\text{H}_2\text{O}$, Ammonium perrhenate NH_4ReO_4 , Cobalt nitrate hexahydrate $\text{Co}(\text{NO}_3)_2 \cdot 6\text{H}_2\text{O}$) were supplied by Sigma-Aldrich (Saint Louis, Missouri, MO, USA) and used with no further purification. The support was Gadolinia 0.2 wt%-Doped Ceria 0.8 wt% (GDC), also supplied by Sigma-Aldrich (Saint Louis, Missouri, MO, USA).

In all ternary catalysts the total metal loading was 50 wt/wt% deposited onto 50 wt/wt% GDC; then, the Nickel loading was 60 wt/wt %, the Molybdenum loading was 30 wt/wt % and the third metal loading (Copper, Rhenium or Cobalt) is 10 wt/wt %.

After impregnation onto the support the catalysts were dried at 120 °C and then calcined at 600 °C for 4 h with a heating rate of 2 °C min^{-1} and cooling rate of 2 °C min^{-1} . Afterwards, they were reduced at 650 °C with H_2 (10 vol.% in He) for 2 h using the same heating and cooling rate as above.

For brevity the catalysts in the text were coded as follows: NiMoRe/GDC, NiMoCu/GDC and NiMoCo/GDC.

3.2. Catalysts Characterization

The phase composition of the fresh and spent catalysts were analyzed by powder X-ray diffraction (XRD) using a Bruker D2 Phaser using Cu $K\alpha$ radiation at 30 kV and 20 mA (Bruker, Karlsruhe, Germany). Peaks attribution was made according with well known databases. The diffraction angles 2θ were varied between 10° and 80° in steps of 0.02° and a count time of 5 s per step.

Temperature programmed reduction (TPR) was carried out with a Chemisorb Micromeritics 2750 instrument (Micromeritics, Norcross, Georgia, GA, USA), to monitor reduction of the metal oxides, under a flux of 50 $\text{cm}^3 \text{min}^{-1}$ of H_2/Ar (10 vol.%) in the temperature range 25–1000 °C at atmospheric pressure.

A Phenom Pro-X scanning electron microscope equipped with an energy-dispersive X-ray (EDX) spectrometer was utilized for SEM analysis (Deben, Suffolk, UK). The EDX analysis was used to evaluate the content and dispersion of metal, acquiring for all sample at least 20 points of investigation for three different magnifications.

The formation of carbonaceous deposits on the surface of the spent catalysts was investigated by measuring Raman scattering. For this purpose, a NT-MDT spectrometer was used. Excitation was provided by a He-Ne laser operating at 1.96 eV (633.8 nm). In order to obtain a sufficient signal to noise ratio, an acquisition time of 15 s was used to record the spectra, which were fit to Gaussian and Lorentzian bands, superimposed to a linear background. A commercially available spectroscopic analysis software package was utilized to choose the center frequency, width (FWHM) and intensity of the bands by a least-square best-fit method.

The amount of carbon deposition on the catalysts was evaluated by isothermal and temperature-programmed TGA/DSC experiments with a Netzsch instrument (Netzsch, Selb, Germany). The temperature-programmed experiments were carried out in air with a total flow rate of 100 $\text{cm}^3 \text{min}^{-1}$, while the loading of the measured samples was approximately 20 mg, with a heating rate of 2 °C min^{-1} .

The transmission electron microscopy (TEM) analysis was carried out using a JEOL 1400 Plus instrument (JEOL USA, Peabody, Massachusetts, MA, USA) operated at 120 kV, able to achieve a 0.19 nm point-to-point resolution and a 0.14 nm line resolution.

Carbon content and sulfur on the spent catalysts surface have been detected by CHNS elemental analysis using a Perkin Elmer 2400 instrument (Perkin Elmer, Waltham, Massachusetts, MA, USA).

3.3. Catalytic Test Measurement

Catalytic activity experiments were performed at atmospheric pressure in a quartz microreactor (internal diameter = 4 mm) placed in a ceramic tube furnace, at a gas hourly space velocity (GHSV) of 120,000 h⁻¹. The catalyst (~50 mg) was placed between quartz wool in the middle of the reactor. The reaction temperature was monitored by a thermocouple inserted into the reactor bed through a quartz tube. The temperature of the reactor bed was kept constant by an electronic controller. The maximum deviation measured in the reactor bed from the nominal temperature was ~10 °C. An isocratic pump (Varian ProStar 210, Varian Inc., Palo Alto, California, CA, USA) connected to an evaporator that was heated at 220 °C, was used to feed water in the gas stream and to control the steam to carbon ratio (S/C) in the reaction gas mixture; N₂ was used as internal standard. The gas lines were heated at 120 °C to prevent condensation. The microreactor was operated in down-flow mode with the gas inlet placed at the top of the reactor.

The catalytic tests were carried out in the range 600–800 °C with steam/carbon and oxygen/carbon ratios equal to 2.5 and 0.5, respectively. All experiments have been carried out with a total inlet flow of 150 cm³ min⁻¹, using nitrogen as balance.

The catalytic tests with sulfur were conducted by introducing different amounts of H₂S (100 or 200 ppm), each one in a different experiment.

Reaction products were analyzed by on-line gas chromatograph (GC Agilent 6590, Agilent, Santa Clara, CA, USA) equipped with FID, FPD and TCD detectors and four columns (Alumina, Porapak Q, Haysep, Molecular Sieves (MS 5A)), for their separation and detection. The catalytic activity results were generally taken 20 min after the reaction conditioning and reproducible data were obtained for registration periods of at least 600 min repeated three times.

Overall carbon and hydrogen balances were close to 100% in each experiment with moderate standard deviation (σ) lower than 3.

4. Conclusions

This study investigated the catalytic performance of trimetallic catalysts, NiMoRe, NiMoCu, and NiMoCo, supported on gadolinia-doped ceria material, in the auto-thermal reforming of ethanol, at two different temperatures, 600 °C and 800 °C. The selectivity of catalysts towards syngas is not affected by the temperature reaction and the total amount of syngas produced ranged between 72 and 77 vol%.

The presence of H₂S in the feed (100 ppm and 200 ppm) increases the selectivity to ethylene and favors aromatic coke deposition. Despite the sulfur presence affecting the products distribution, no severe catalysts deactivation occurred: the hydrogen selectivity decreased, but total ethanol conversion was, however, observed.

Among the catalysts tested, NiMoCu/GDC appears to be less sensitive to the sulfur presence and shows the best selectivity to hydrogen.

Supplementary Materials: The following are available online at <http://www.mdpi.com/2073-4344/8/10/435/s1>, Figure S1. SEM-EDX images of NiMoCo/GDC catalyst surface (representative sample) –(a) after impregnation; (b) after calcination, Figure S2. Elements mapping of NiMoCo/GDC catalyst surface after activation (representative sample), Figure S3. Selectivity to syngas (H₂ + CO) of different catalysts, at 600 °C and 800 °C, after 10 h, 120,000 h⁻¹ space velocity, Figure S4. Thermal profiles, TG (black line) DSC (dotted line), of NiMoCu/GDC catalyst after ATR of ethanol at T = 600 °C, as representative sample, Figure S5. XRD spectrum of NiMoRe/GDC spent catalyst after 10 h of ATR at T = 600 °C, without H₂S in the feed (representative sample), Figure S6. Correlation between the average intensity of the Csp² related Raman bands and the relative amount of deposited carbon, as assessed by thermo-gravimetric analysis.

Author Contributions: Conceptualization, P.F., A.M. and P.A.; Formal analysis, S.S.; Investigation, A.M., S.S., C.T. and F.C.; Project administration, P.F. and A.M.; Supervision, P.F., A.M. and P.A.; Writing – original draft, P.F. and A.M.; Writing – review & editing, P.F., A.M., A.M. and P.A.

Funding: This research was funded by Ministry of Education, Universities and Research (Italy): PRIN 2010/2011 - Topic: Solid oxide fuel cells operating at intermediate temperature fed with biofuels (BIOITSOFC), Ministry of Economic Development joint CNR DIITET: Sistemi elettrochimici per l'accumulo di energia/ Electrochemical systems for energy storage.

Acknowledgments: The Authors would like to thank Dr. Daniela Perrota, of University of Calabria, TEM laboratory of DiBest, for her contribution to the TEM characterization.

Conflicts of Interest: The authors have no conflict of interest to declare.

References

1. Jamsak, W.; Assabumrungrat, S.; Douglas, P.L.; Laosiripojana, N.; Charojrochkul, S. Theoretical performance analysis of ethanol-fuelled solid oxide fuel cells with different electrolytes. *Chem. Eng. J.* **2006**, *119*, 11–18. [[CrossRef](#)]
2. Deluga, G.A.; Salge, J.R.; Schmidt, L.D.; Verykios, X.E. Renewable hydrogen from ethanol by autothermal reforming. *Science* **2004**, *303*, 993–997. [[CrossRef](#)] [[PubMed](#)]
3. Perkas, N.; Amirian, G.; Zhong, Z.; Teo, J.; Gofer, Y.; Gedanken, A. Methanation of carbon dioxide on Ni catalysts on mesoporous ZrO₂ doped with rare earth oxides. *Catal. Lett.* **2009**, *130*, 455–462. [[CrossRef](#)]
4. Ni, M.; Leung, D.Y.C.; Leu, M.K.H. A review on reforming bio-ethanol for hydrogen production. *Int. J. Hydrog. Energy* **2007**, *32*, 3238–3247. [[CrossRef](#)]
5. Frontera, P.; Macario, A.; Monforte, G.; Bonura, G.; Ferraro, M.; Dispenza, G.; Antonucci, V.; Aricò, A.S.; Antonucci, P.L. The role of Gadolinia Doped Ceria support on the promotion of CO₂ methanation over Ni and Ni-Fe catalysts. *Int. J. Hydrog. Energy* **2017**, *42*, 26828–26842. [[CrossRef](#)]
6. Le, M.C.; Van, K.L.; Nguyen, T.H.T.; Nguyen, N.H. The impact of Ce-Zr addition on nickel dispersion and catalytic behavior for CO₂ methanation of Ni/AC catalyst at low temperature. *J. Chem.* **2017**. [[CrossRef](#)]
7. Frontera, P.; Macario, A.; Ferraro, M.; Antonucci, P.L. Supported catalysts for CO₂ methanation: A review. *Catalysts* **2017**, *7*, 59. [[CrossRef](#)]
8. Han, S.J.; Bang, Y.J.; Seo, J.G.; Yoo, J.; Song, I.K. Hydrogen production by steam reforming of ethanol over mesoporous Ni–Al₂O₃–ZrO₂ xerogel catalysts: Effect of Zr/Al molar ratio. *Int. J. Hydrog. Energy* **2013**, *38*, 1376–1383. [[CrossRef](#)]
9. Candamano, S.; Frontera, P.; Macario, A.; Crea, F.; Nagy, J.B.; Antonucci, P.L. Preparation and characterization of active Ni-supported catalyst for syngas production. *Chem. Eng. Res. Des.* **2015**, *96*, 78–86. [[CrossRef](#)]
10. Chen, H.Q.; Yu, H.; Yang, G.X.; Peng, F.; Wang, H.J.; Wang, J. Auto-thermal ethanol micro-reformer with a structural Ir/La₂O₃/ZrO₂ catalyst for hydrogen production. *Chem. Eng. J.* **2011**, *167*, 322–327. [[CrossRef](#)]
11. Mauriello, F.; Paone, E.; Pietropaolo, R.; Balu, A.M.; Luque, R. Catalytic Transfer Hydrogenolysis of Lignin-Derived Aromatic Ethers Promoted by Bimetallic Pd/Ni Systems. *ACS Sustain. Chem. Eng.* **2018**, *6*, 9269–9276. [[CrossRef](#)]
12. Siang, T.J.; Pham, T.L.M.; Cuong, N.V.; Phuong, P.T.T.; Phuc, N.H.H.; Truong, Q.D.; Vo, D.V.N. Combined steam and CO₂ reforming of methane for syngas production over carbon-resistant boron-promoted Ni/SBA-15 catalysts. *Mesoporous Mesoporous Mater.* **2018**, *262*, 122–132. [[CrossRef](#)]
13. Frontera, P.; Aloise, A.; Macario, A.; Crea, F.; Antonucci, P.L.; Giordano, G.; Nagy, J.B. Zeolite-supported Ni catalyst for methane reforming with carbon dioxide. *Res. Chem. Intermed.* **2011**, *37*, 267–279. [[CrossRef](#)]
14. Baruah, R.; Dixit, M.; Basarkar, P.; Parikh, D.; Bhargava, A. Advances in ethanol autothermal reforming. *Renew. Sustain. Energ. Rev.* **2015**, *51*, 1345–1353. [[CrossRef](#)]
15. Chen, H.; Yu, H.; Tang, Y.; Pan, M.; Yang, G.; Peng, F.; Wang, H.; Yang, J. Hydrogen production via autothermal reforming of ethanol over noble metal catalysts supported on oxides. *J. Nat. Gas Chem.* **2009**, *18*, 191–198. [[CrossRef](#)]
16. Chen, H.; Yu, H.; Peng, F.; Yang, G.; Wang, H.; Yang, J.; Tang, Y. Autothermal reforming of ethanol for hydrogen production over perovskite LaNiO₃. *Chem. Eng. J.* **2010**, *160*, 333–339. [[CrossRef](#)]
17. Frontera, P. Alkaline-promoted zeolites for methane dry-reforming catalyst preparation. *Adv. Sci. Lett.* **2017**, *23*, 5883–5885. [[CrossRef](#)]
18. Frusteri, F.; Arena, F.; Calogero, G.; Torre, T.; Parmaliana, A. Potassium-enhanced stability of Ni/MgO catalysts in the dry-reforming of methane. *Catal. Commun.* **2001**, *2*, 49–56. [[CrossRef](#)]

19. Ghani, A.A.; Torabi, F.; Ibrahim, H. Autothermal reforming process for efficient hydrogen production from crude glycerol using nickel supported catalyst: Parametric and statistical analyses. *Energy* **2018**, *144*, 129–145. [[CrossRef](#)]
20. Frontera, P.; Macario, A.; Candamano, S.; Barberio, M.; Crea, F.; Antonucci, P.L. CO₂ conversion over supported Ni nanoparticles. *Chem. Eng. Trans.* **2017**, *60*, 229–234.
21. Palma, V.; Ruocco, C.; Meloni, E.; Ricca, A. Activity and stability of novel silica-based catalysts for hydrogen production via oxidative steam reforming of ethanol. *Chem. Eng. Trans.* **2016**, *52*, 67–72.
22. Pandey, D.; Deo, G. Effect of support on the catalytic of supported Ni-Fe catalysts for CO₂ methanation reaction. *J. Ind. Eng. Chem.* **2016**, *33*, 99–107. [[CrossRef](#)]
23. Wang, C.H.; Ho, K.F.; Chiou, J.Y.Z.; Lee, C.L.; Yang, S.Y.; Yeh, C.T.; Wang, C.B. Oxidative steam reforming of ethanol over PtRu/ZrO₂ catalysts modified with sodium and magnesium. *Catal. Commun.* **2011**, *12*, 854–858. [[CrossRef](#)]
24. Kugai, J.; Subramani, V.; Song, C.; Engelhard, M.H.; Chin, Y.H. Effects of nanocrystalline CeO₂ supports on the properties and performance of Ni–Rh bimetallic catalyst for oxidative steam reforming of ethanol. *J. Catal.* **2006**, *238*, 430–440. [[CrossRef](#)]
25. Gutierrez, A.; Karinen, R.; Airaksinen, S.; Kaila, R.; Krause, A.O.I. Autothermal reforming of ethanol on noble metal catalysts. *Int. J. Hydrog. Energy* **2011**, *36*, 8967–8977. [[CrossRef](#)]
26. Lin, W.H.; Liu, Y.C.; Chang, H.F. Autothermal reforming of ethanol in a Pd–Ag/Ni composite membrane reactor. *Int. J. Hydrog. Energy* **2010**, *35*, 12961–12969. [[CrossRef](#)]
27. Wu, H.; Pantaleo, G.; La Parola, V.; Venezia, A.M.; Collard, X.; Aprile, C.; Liotta, L.F. Bi- and trimetallic Ni catalysts over Al₂O₃ and Al₂O₃-MO_x (M = Ce or Mg) oxides for methane dry reforming: Au and Pt additive effects. *Appl. Catal. B Environ.* **2014**, *156–157*, 350–361. [[CrossRef](#)]
28. Kozlov, A.I.; Kim, D.H.; Yezerets, A.; Anderson, P.; Kung, H.H.; Kung, M.C. Effect of preparation method and redox treatment on the reducibility and structure of supported Ceria-Zirconia Mixed Oxide. *J. Catal.* **2002**, *209*, 417–426. [[CrossRef](#)]
29. Hwang, S.; Hong, U.G.; Lee, J.; Seo, J.G.; Baik, J.H.; Koh, D.J.; Lim, H.; Song, I.K. Methanation of carbon dioxide over mesoporous Ni-Fe-Al₂O₃ catalysts prepared by a coprecipitation method: Effect of precipitation agent. *Int. Eng. Chem.* **2013**, *19*, 2016–2021. [[CrossRef](#)]
30. Ashok, J.; Ang, M.L.; Kawi, S. Enhanced activity of CO₂ methanation over Ni/CeO₂-ZrO₂ catalysts: Influence of preparation methods. *Catal. Today* **2017**, *281*, 304–311. [[CrossRef](#)]
31. Lohsoontorn, P.; Brett, D.J.L.; Brandon, N.P. Thermodynamic predictions of the impact of fuel composition on the propensity of sulphur to interact with Ni and ceria-based anodes for solid oxide fuel cells. *J. Power Sources* **2008**, *175*, 60–67. [[CrossRef](#)]
32. Kesavan, J.K.; Luisetto, I.; Tuti, S.; Meneghini, C.; Iucci, G.; Battocchio, C.; Mobilio, S.; Casciardi, S.; Sisto, R. Nickel supported on YSZ: The effect of Ni particle size on the catalytic activity for CO₂ methanation. *J. CO₂ Util.* **2018**, *23*, 200–211. [[CrossRef](#)]
33. Lo Faro, M.; Modafferri, V.; Frontera, P.; Antonucci, P.L.; Aricò, A.S. Catalytic behavior of Ni-modified perovskite and doped ceria composite catalyst for the conversion of odorized propane to syngas. *Fuel Process. Technol.* **2013**, *113*, 28–33. [[CrossRef](#)]
34. An, W.; Gatewood, D.; Dunlap, B.; Turner, C.H. Catalytic activity of bimetallic nickel alloys for solid-oxide fuel cell anode reactions from density-functional theory. *J. Power Sources* **2006**, *159*, 68–72. [[CrossRef](#)]
35. Fu, C.J.; Chan, S.H.; Ge, X.M.; Liu, Q.L.; Pasciak, G. A promising Ni-Fe bimetallic anode for intermediate-temperature SOFC based on Gd-doped ceria electrolyte. *Int. J. Hydrog. Energy* **2011**, *36*, 13727–13734. [[CrossRef](#)]
36. Paik, S.C.; Chung, J.S. Selective catalytic reduction of sulfur dioxide with hydrogen to elemental sulfur over Co-Mo/Al₂O₃. *Appl. Catal. B Environ.* **1995**, *5*, 233–243. [[CrossRef](#)]
37. Alvarez, E.; Mendioroz, S.; Palacios, J.M. Catalyst for the elimination of sulfur dioxide from stream by the Claus reaction at low temperature. *Appl. Catal. A Gen.* **1993**, *93*, 231–244. [[CrossRef](#)]
38. Borchert, H.; Borchert, Y.; Kaichev, V.V.; Prosvirin, I.P.; Alikina, G.M.; Lukashovich, A.I.; Zaikovskii, V.I.; Moroz, E.M.; Paukshtis, E.A.; Bukhtiyarov, V.I.; et al. Nanostructured, Gd-doped ceria promoted by Pt or Pd: Investigation of the electronic and surface structures and relations to chemical properties. *J. Phys. Chem. B* **2005**, *109*, 20077–20086. [[CrossRef](#)] [[PubMed](#)]
39. Brito, J.L.; Laine, J. Reducibility of Ni-Mo/Al₂O₃ catalysts: A TPR study. *J. Catal.* **1993**, *139*, 540–550. [[CrossRef](#)]

40. Pastor-Pérez, L.; Le Saché, E.; Jones, C.; Gu, S.; Arellano-Garcia, H.; Reina, T.R. Synthetic natural gas production from CO₂ over Ni-x/CeO₂-ZrO₂ (x = Fe, Co) catalysts: Influence of promoters and space velocity. *Catal. Today* **2017**. [[CrossRef](#)]
41. Çağlayan, B.S.; Aksoylu, A.E. Water gas shift activity of ceria supported Au-Re catalysts. *Catal. Commun.* **2011**, *12*, 1206–1211. [[CrossRef](#)]
42. Sagar, G.V.; Rao, P.V.; Srikanth, C.S.; Chary, K.V. Dispersion and reactivity of copper catalysts supported on Al₂O₃-ZrO₂. *J. Phys. Chem. B* **2006**, *110*, 13381–13388. [[CrossRef](#)] [[PubMed](#)]
43. Lo Faro, M.; Frontera, P.; Antonucci, P.L.; Aricò, A.S. Ni-Cu based catalysts prepared by two different methods and their catalytic activity toward the ATR of methane. *Chem. Eng. Res. Des.* **2015**, *93*, 269–277. [[CrossRef](#)]
44. Liu, H.; Yin, C.; Li, H.; Liu, B.; Li, X.; Chai, Y.; Li, Y.; Liu, C. Synthesis, characterization and hydrodesulfurization properties of nickel–copper–molybdenum catalysts for the production of ultra-low sulfur diesel. *Fuel* **2014**, *129*, 138–146. [[CrossRef](#)]
45. Laiyuan, C.; Yuequin, N.; Jingling, Z.; Liwu, L. Role of sulfur in a skewed reforming catalyst with a low platinum content and a high rhenium-to-platinum ratio. *Appl. Catal. A Gen.* **1993**, *97*, 133–143. [[CrossRef](#)]
46. Rodríguez-Castellón, E.; Jiménez-López, A.; Eliche-Quesada, D. Nickel and cobalt promoted tungsten and molybdenum sulfide mesoporous catalysts for hydrodesulfurization. *Fuel* **2008**, *87*, 1195–1206. [[CrossRef](#)]
47. Lakhapatri, S.L.; Abraham, M.A. Deactivation due to sulfur poisoning and carbon deposition on Rh-Ni/Al₂O₃ catalyst during steam reforming of sulfur-doped n-hexadecane. *Appl. Catal. A* **2009**, *364*, 113–121. [[CrossRef](#)]
48. Froment, G.F. Production of synthesis gas by steam- and CO₂-reforming of natural gas. *J. Mol. Catal. A Chem.* **2000**, *163*, 147–156. [[CrossRef](#)]
49. Simson, A.; Crowley, S.; Castaldi, M.J. The impact of sulfur on ethanol steam reforming. *Catal. Lett.* **2016**, *146*, 1361–1372. [[CrossRef](#)]
50. Bion, N.; Duprez, D.; Epron, F. Design of nanocatalysts for green hydrogen production from bioethanol. *ChemSusChem* **2012**, *5*, 76–84. [[CrossRef](#)] [[PubMed](#)]
51. Ferrari, A.C.; Robertson, J. Raman spectroscopy in carbons: From nanotubes to diamond. *Philos. Trans. R. Soc. A* **2004**, *362*, 2269–2565. [[CrossRef](#)]
52. Gallo, A.; Pirovano, C.; Ferrini, P.; Marelli, M.; Psaro, R.; Santangelo, S.; Faggio, G.; Dal Santo, V. Influence of reaction parameters on the activity of ruthenium based catalysts for glycerol steam reforming. *Appl. Catal. B Environ.* **2012**, *121–122*, 40–49. [[CrossRef](#)]
53. Santangelo, S. Controlled surface functionalisation of carbon nanotubes by nitric acid vapors generated from sub-azeotropic solution. *Surf. Interface Anal.* **2016**, *48*, 17–25. [[CrossRef](#)]
54. Ferrari, A.C.; Robertson, J. Interpretation of Raman spectra of disordered and amorphous carbon. *Phys. Rev. B* **2000**, *61*, 14095–14107. [[CrossRef](#)]
55. Ferrari, A.C.; Robertson, J. Resonant Raman spectroscopy of disordered, amorphous, and diamondlike carbon. *Phys. Rev. B* **2001**, *64*. [[CrossRef](#)]
56. Thomsen, C.; Reich, S. Double Resonant Raman Scattering in Graphite. *Phys. Rev. Lett.* **2000**, *85*, 5214–5217. [[CrossRef](#)] [[PubMed](#)]
57. Messina, G.; Santangelo, S. Multi-wavelength Raman investigation of sputtered a-C film nanostructure. *Surf. Coat. Technol.* **2006**, *200*, 5427–5434. [[CrossRef](#)]
58. Ferrari, A.C.; Kleinsorge, B.; Adamopoulos, G.; Robertson, J.; Milne, W.I.; Stolojan, V.; Brown, L.M.; Li Bassi, A.; Tanner, B.K. Stress reduction and bond stability during thermal annealing of tetrahedral amorphous carbon. *J. Appl. Phys.* **1999**, *85*, 7191–7197. [[CrossRef](#)]
59. Cai, W.; Ramirez de la Piscina, P.; Homs, N. Hydrogen production from the steam reforming of bio-butanol over novel supported Co-based bimetallic catalysts. *Biores. Technol.* **2012**, *107*, 482–486. [[CrossRef](#)] [[PubMed](#)]
60. Rakass, S.; Oudghiri-Hassani, H.; Abatzoglou, N.; Rowntree, P. A study of the surface properties and steam reforming catalytic activity of nickel powders impregnated by n-alkanethiols. *J. Power Sources* **2006**, *162*, 579–588. [[CrossRef](#)]

